

Lead Halide Perovskite-Based Dynamic Metasurfaces

Chen Zhang, Shumin Xiao,* Yuhan Wang, Yisheng Gao, Yubin Fan, Can Huang, Nan Zhang, Wenhong Yang, and Qinghai Song*

Lead halide perovskites $\text{CH}_3\text{NH}_3\text{PbX}_3$ (MAPbX₃) are known to have high refractive index and controllable bandgap, making them attractive for all-dielectric and tunable metasurfaces. Till now, perovskite metasurfaces have only been used in structural colors. More interesting meta-devices with 2π phase control are still absent. Here, MAPbX₃-perovskite-based metasurfaces are experimentally demonstrated with a complete control of phase shift in a reflection mode. By utilizing MAPbBr₃ cut-wires as meta-atoms on a ground metal film, it is found that the MAPbBr₃ perovskite metasurface can produce full phase control from 0 to 2π and high reflection efficiency simultaneously. Consequently, high-efficiency polarization conversion, anomalous reflection, and meta-holograms are successfully produced. Most interestingly, the bandgap of the MAPbX₃ perovskite can be post-synthetically and reversibly tuned via anion exchange, providing a new approach to dynamically control of the all-dielectric meta-devices with novel function such as anomalous reflection and hologram.

materials such as titanium dioxides (TiO₂), silicon nitrides (Si₃N₄), and gallium nitride (GaN) have been applied to replace silicon, germanium, and plasmonic materials for the realization of the meta-devices in the visible spectrum.^[16–21] Functional devices including metalens, color printer, hologram, and even achromatic lens have also been successfully demonstrated.^[16–24] However, due to their relatively stable properties, the optical performances of such meta-devices are typically fixed and hard to be post-fabrication tuned once they are fabricated as their counterparts made of plasmonic or phase-transition material, for example, Mg, Pb, VO₂, ITO etc.^[25–28] Although infiltrating different solutions can partially tune the optical characteristics, the reduced refractive

1. Introduction


Metasurface is a type of novel 2D system that is composed of subwavelength scale antennas.^[1–8] Compared with their uniform counterparts, metasurfaces can accurately control the amplitude, phase, and polarization of the transmitted or reflected light.^[9–12] In the past few years, a large number of unique functionalities and optical components such as flat lens, holograms, and gratings have been demonstrated in plasmonic metasurfaces and high refractive index dielectric (Si, Ge) metasurfaces.^[12–15] Recently, in order to overcome the intrinsic losses, transparent

index contrast significantly affect their abilities in fully controlling the phase shift from 0 to 2π .^[29,30]

Solution-processed lead halide perovskites (MAPbX₃, X = I, Cl, Br, and their mixtures) have recently emerged as a class of promising semiconductors for cost-effective optoelectronic devices.^[31,32] Due to the long carrier diffusion length, low defect density, high carrier mobility, and widely tunable bandgap, the photon conversion efficiency (PCE) of lead halide perovskite-based solar cell has been dramatically increased from 3.8% to 23.1% in a few years.^[33] Perovskite-based photodetectors, light-emitting diodes, and microlasers have also been rapidly developed simultaneously.^[34–45] Recently, lead halide perovskites started to show their potential in metasurfaces and metamaterials.^[46–49] Their refractive indices ($n \approx 2.2$ – 2.55) are comparable to or much larger than conventional transparent materials.^[50] And a series of nanofabrication techniques have been developed to convert the solution-processed materials into perovskite nano-structures, for example, focused ion beam milling (FIB), electron beam lithography (EBL), nano-imprinting, and inductively coupled plasma (ICP) etching.^[51–53] Up to now, perovskite-based metasurfaces have been successfully fabricated for high-resolution color and dynamic nano-printings.^[47–49] Recently, the dynamically reconfigurable resonant modes have also been realized in perovskite nanoparticles by controlling the stoichiometry via the anion exchange.^[54] However, the more challenging experiments such as complete control of phase shift from 0 to 2π and functional devices such as metalens and meta-hologram are still absent. Herein, we report the MAPbX₃ perovskite metasurfaces with complete phase control and explore their potential in dynamic meta-devices.

Dr. C. Zhang, Prof. S. M. Xiao, Dr. Y. H. Wang, Dr. Y. S. Gao, Dr. Y. B. Fan, Dr. C. Huang, Dr. N. Zhang, Dr. W. H. Yang, Prof. Q. H. Song
State Key Laboratory on Tunable Laser Technology
Ministry of Industry and Information Technology Key Lab of Micro-Nano Optoelectronic Information System
Shenzhen Graduate School
Harbin Institute of Technology
Shenzhen, 518055, P. R. China
E-mail: shumin.xiao@hit.edu.cn; qinghai.song@hit.edu.cn

Dr. C. Zhang, Prof. S. M. Xiao, Dr. Y. H. Wang, Dr. Y. S. Gao, Dr. Y. B. Fan, Dr. C. Huang, Dr. N. Zhang, Dr. W. H. Yang, Prof. Q. H. Song
Collaborative Innovation Center of Extreme Optics
Shanxi University
Taiyuan, 030006, Shanxi, P. R. China

 The ORCID identification number(s) for the author(s) of this article can be found under <https://doi.org/10.1002/lpor.201900079>

DOI: 10.1002/lpor.201900079

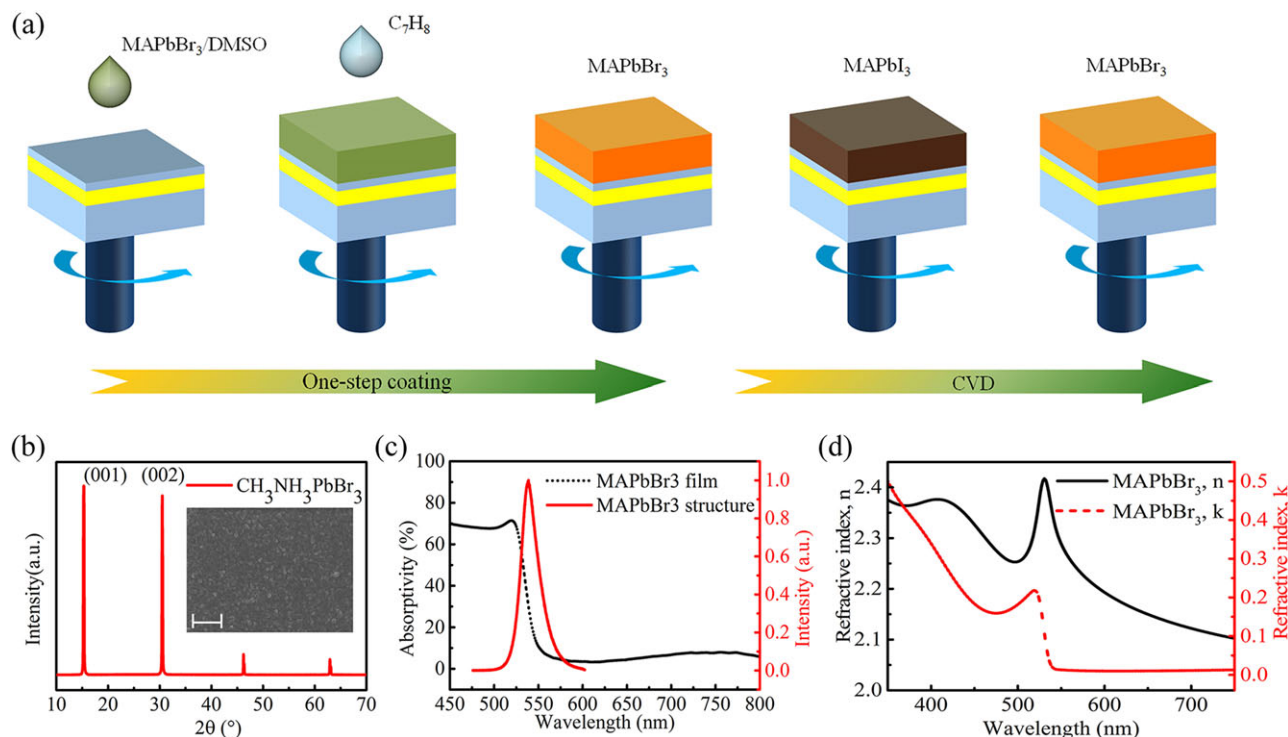


Figure 1. The lead halide perovskite (MAPbX₃) films. a) The schematic picture of synthesis process. b) The XRD spectra for the as-grown MAPbBr₃ perovskite film. The inset is the top-view SEM image of the MAPbBr₃ film. The scale bar is 1 μm. (c) and (d) show the corresponding absorption and fluorescence spectra and *n*, *k* of MAPbBr₃ perovskite films.

2. Results and Discussions

2.1. Synthesis and Characterization of Lead Halide Perovskite Film

The whole experiment started with a MAPbBr₃ film on a gold film, separated by a SiO₂ spacer. Basically, a 100-nm gold reflection mirror and a 20-nm SiO₂ protecting layer were deposited onto a glass substrate via electron beam (E-beam) evaporation. The deposition rates were 0.04 and 0.05 nm s⁻¹, respectively. The MAPbBr₃ film was prepared by spin-coating a solution containing PbBr₂ and MABr in a mixture solvent of N,N-dimethylformamide (DMF) and dimethyl sulfoxide (DMSO) (see Figure 1a and Experimental section).^[55] Here the SiO₂ spacer was applied to protect the gold film and to improve the quality of MAPbBr₃ film. The top-view scanning electron microscope (SEM) image (inset in Figure 1b) shows that the synthesized perovskite film is quite uniform and no obvious pinholes can be observed. The grain sizes are on the order of 100 nm. The root mean square value of surface roughness, characterized with atomic force microscope (AFM), is less than 7.2 nm (see Figure S4a, Supporting Information). Figure 1b shows the X-ray diffraction (XRD) spectrum of the film. Four obvious peaks can be clearly seen at 15.3°, 30.5°, 46.2°, and 62.9°, corresponding to (001), (002), (003), and (004) planes of cubic phase MAPbBr₃ well.^[56] By fitting the absorption curve in Figure 1c the bandgap of MAPbBr₃ perovskite can be determined around 2.25 eV (The detail fitting result see Figure S4b, Supporting Information). The refractive index (*n*) and extinction coefficient (*k*) of MAPbBr₃ were also mea-

sured and plotted in Figure 1d. The refractive index of MAPbBr₃ is well above 2.1 in the entire visible spectrum (400–700 nm).

2.2. Perovskite Metasurface-Based Polarization Conversion, Anomalous Reflection, and Hologram

The high refractive index, relatively large bandgap, and good quality make MAPbBr₃ perovskite films very promising for applications in all-dielectric nano-photonics, especially for the spectral range below the bandgap. Metasurface-based broad-band and high-efficiency polarization converter is one good example.^[57] Here we take the cut-wire based metasurface as an example to illustrate this possibility. As the SEM image and schematic picture shown in Figure 2a,b, the length and width of each cut-wire are *a* = 160 nm and *b* = 295 nm, respectively. The periods in both directions are 510 nm and the thickness of perovskite cut-wire, measured by profilometry, is 300 nm. Such kinds of perovskite cut-wires are large enough to support resonances along both of long and short axes.^[58] For incident light with polarization along *x* or *y* directions, it can be decomposed into two perpendicular components along the long and short axes (see Figure 2b). As the resonances along two axes are different (see Figure S5, Supporting Information), the phase retardation between two components are generated. For the current cut-wires, the phase retardation has been numerically optimized to π for a wide spectral range (Figure 2c). In this sense, the direction of one component shall be reversed and thus the polarization of reflected light is rotated

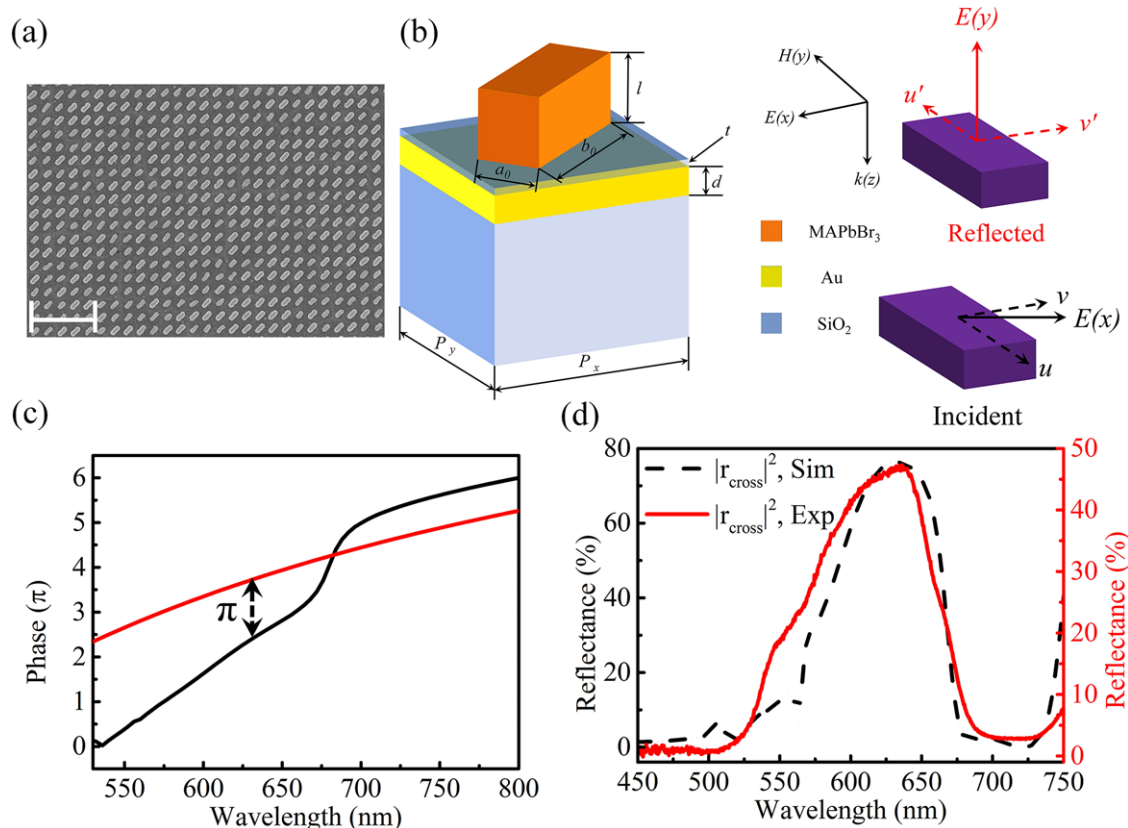


Figure 2. The MAPbBr₃ metasurface based polarization converter. a) The tilt-view SEM image of the perovskite metasurface. The scale bar is 2 μm . b) The illustration of polarization rotation via phase retardation. c) The phase retardation between two components along long and short axes. d) The numerically calculated and experimentally recorded reflection spectra for cross-polarization.

90° (see right panel in Figure 2b). The dashed line in Figure 2d shows the numerically calculated reflection spectrum with cross polarization. The cross-polarized reflection remains above 90% in a wide range from 540 to 680 nm, consistent with the phase retardation in Figure 2c very well.

Then the MAPbBr₃ perovskite metasurface was created by patterning the perovskite film into cut-wires via E-beam lithography and reactive ion etching (see details in Experimental section). The SEM image of the perovskite metasurface (see Figure 2a) shows that all the structural parameters follow the design very well and no residuals can be observed after the ICP etching. The optical properties of perovskite metasurface have been examined with a white-light source and a CCD camera coupled spectrometer (see Experimental section). The experimental results are summarized as solid line in Figure 2d. Similar to the numerical calculations, a high-efficiency and broadband polarization reflection spectrum for cross-polarization has been successfully generated with the MAPbBr₃ perovskite metasurface. The experimentally recorded absolute efficiency ($\eta = |r_{\text{cross}}|^2 / I_{\text{incident}}$) was around 45%, which was slightly lower than the numerical calculation. From the high-resolution SEM image (see Figure S7, Supporting Information), we know that fabricated cut-wires still have relatively rough boundaries, which are very similar to the initial grain size in Figure 1b. This might be caused by different etching speed along different crystal directions in MAPbBr₃ perovskites and it can be removed if single-crystalline film is applied. However,

if we define the polarization conversion efficiency following the previous reports ($\eta = |r_{\text{cross}}|^2 / (|r_{\text{cross}}|^2 + |r_{\text{co}}|^2)$), the experimentally recorded value was above 80% from 525 to 650 nm (see Figure S6, Supporting Information), which is comparable to the recent literatures with silicon and TiO₂.^[57] Thus we confirm that lead halide perovskite is a good candidate for all-dielectric meta-devices and their performances can be further improved if single crystalline lead halide perovskite is applied. We note that the phase retardation is determined by the different resonances along long and short axes. The sizes and shapes of cut-wires must be precisely controlled. In this sense, while some other techniques can also produce perovskite nanoparticles with Mie resonances, their random sizes and shapes exclude them from the applications in perovskite metasurfaces.

In addition to the phase retardation, the perovskite cut-wires can also produce phase shift between incident light and the reflected light. Interestingly, this kind of phase shift is found to be dependent on the structural parameters. The colormaps in Figure 3a,b summarize the numerically calculated polarization conversion efficiency (here and below we use the absolute efficiency) and the corresponding phase shift as a function of a and b , respectively. A region with high reflectance ($|r_{\text{cross}}|^2 \approx 65\text{--}80\%$) can be clearly seen in Figure 3a. Within this region, it is easy to select four cut-wires (see open circles in Figure 3b and schematic picture in Figure 3c) to provide an incremental phase shift of $\pi/4$ for the cross-polarized reflected light. An additional

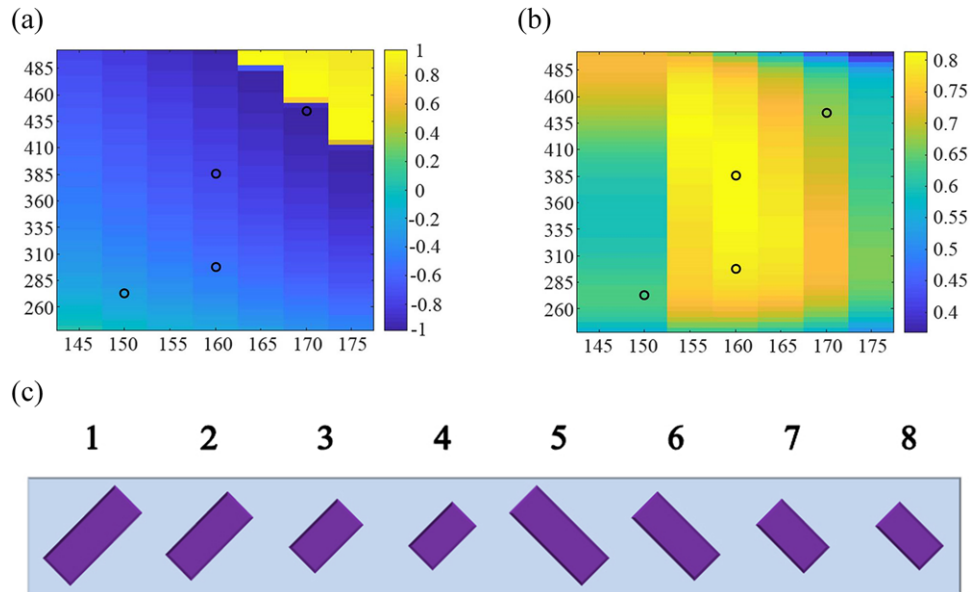


Figure 3. Numerically simulated cross-polarized reflection. (a) and (b) are the reflectance and phase of cut-wires with varying size parameter a and b . Here the incident laser is fixed at 632.8 nm for He-Ne laser. c) The selected cut-wires in (b) for realization of 0 – 2π phase control.

π phase shift can be attained by rotating the cut-wire 90° , simply realizing the full 2π coverage and high polarization conversion efficiency simultaneously.

In order to validate the 2π full coverage of phase shift, we have fabricated a metasurface composed of eight cut-wires in Figure 3c with the same nanofabrication technique as the above. Figure 4a shows the top-view SEM image of the perovskite metasurface. We can see that eight resonators are placed one another forming a linear phase gradient over a supercell with length $L = 4.08 \mu\text{m}$. The numerical calculation in Figure 4b shows that the light is anomalously reflected when it illuminates the metasurface at normal incidence. The anomalous reflection angle $r = 8.91^\circ$ in Figure 4c matches the equation derived from generalized Snell's law $\theta_r = \sin^{-1}[(\lambda_0/nL) + \sin(\theta_i)]$, here $i = 0^\circ$ is the incident angle. The corresponding experimental results are summarized in Figure 4d. When the perovskite metasurface was illuminated with a x -polarized He-Ne laser at normal incidence, two reflected laser spots have been experimentally recorded (see the setup in methods and Figure S3, Supporting Information). The co-polarized one was the normal reflection, whereas the cross-polarized one corresponded to the anomalous reflection. Here the recorded coefficient of anomalous reflection is about 46%, consistent with the polarization conversion in Figure 2 well. Interestingly, the anomalous reflection here also clearly demonstrates the potential of perovskites in meta-lens. Similar to the polarization conversion, the sizes and shapes of cut-wires must be very close to the designs in Figure 3c. The deviations in cut-wires will degrade or smear out the designed function.

The full coverage of phase shift is also important for the computer-generated hologram (CGH). Based on the selected cut-wires in Figure 3c, we have designed a cross-polarized hologram with the Gerchberg–Saxton algorithm (see detail phase distribution in Figure S9, Supporting Information). The schematic picture is depicted in Figure 5a. When a He-Ne laser is illuminated onto the sample at normal incidence, an off-axis and cross-

polarized holographic image of “HIT” (the abbreviation of our university name, Harbin Institute of Technology) has been generated. The phase distribution of hologram, which is optimized by considering the polarization conversion, signal-to-noise ratio, and uniformity, have been calculated and experimentally endowed to perovskite cut-wires via nanofabrication. The total size of perovskite metasurface is $410 \mu\text{m} \times 410 \mu\text{m}$. The enlarged top-view SEM image is shown in Figure 5b, where eight types of cut-wires in Figure 3c have been fully utilized. Then the metasurface was illuminated with a x -polarized He-Ne laser and its y -polarized reflection image was recorded by a CCD camera. As shown in Figure 5c, a bright “HIT” can be clearly seen, consistent with the numerical simulation well. The efficiency of anomalous reflection, which is defined as $\eta_{\text{hologram}} = I_{\text{hologram}}/I_{\text{incident}}$, was about 22.02%. This value is already much higher than the values of plasmonic metasurface or Si metasurface based holograms.

2.3. Dynamic Anomalous Reflection and Hologram

From the above results, we know that the lead halide perovskites can be utilized as functional meta-devices and their performances are as good as conventional metasurfaces. However, the most intriguing properties of lead halide perovskites have not been fully exploited yet. Compared with the conventional semiconductors, the optical properties such as bandgap of lead halide perovskite are post-synthetically controllable with many techniques, making dielectric metasurfaces dynamically and reversibly controllable as their plasmonic counterparts as well. Here the perovskites are tuned with the anion exchange in a chemical vapor deposition (CVD) tube,^[51] (see details in Experimental section and Figure S1, Supporting Information). Figure 6a shows the experimentally recorded XRD spectrum after the anion exchange with MAI vapor. The peaks at 15.3° , 30.5° , 46.2° , and 62.9° in Figure 1b all disappeared and a series of

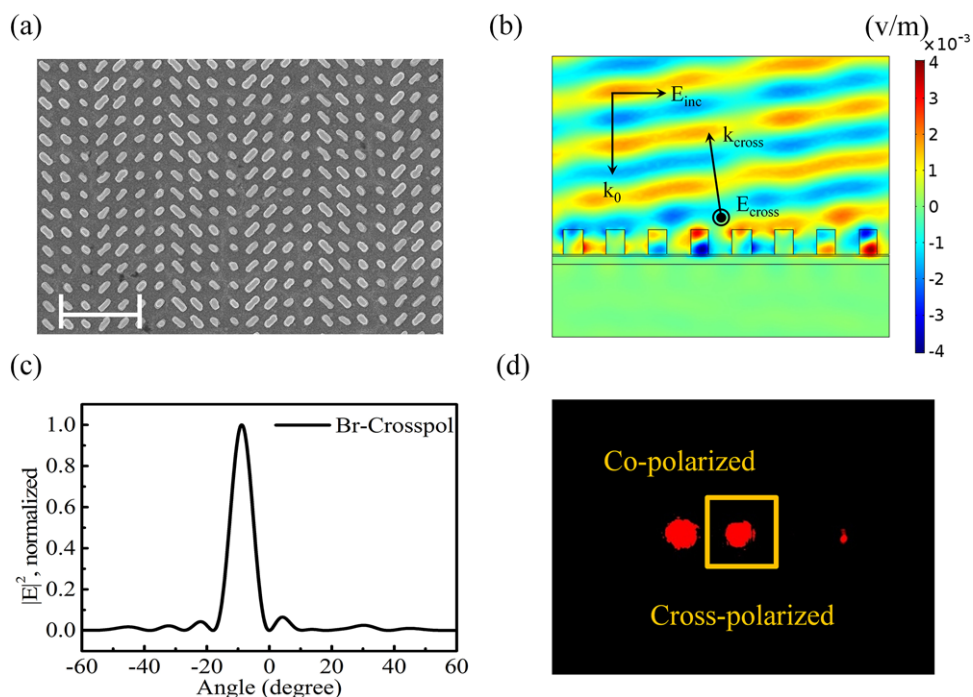


Figure 4. Dynamic anomalous reflection. a) The top-view SEM image of MAPbBr₃ metasurface. The scale bar is 2 μm. b) The field distributions of MAPbBr₃ perovskite metasurface illuminated with a He-Ne laser at normal incidence. c) The calculated far field angular distributions of anomalous reflection for MAPbBr₃ metasurface. d) The corresponding experiment results of anomalous reflection.

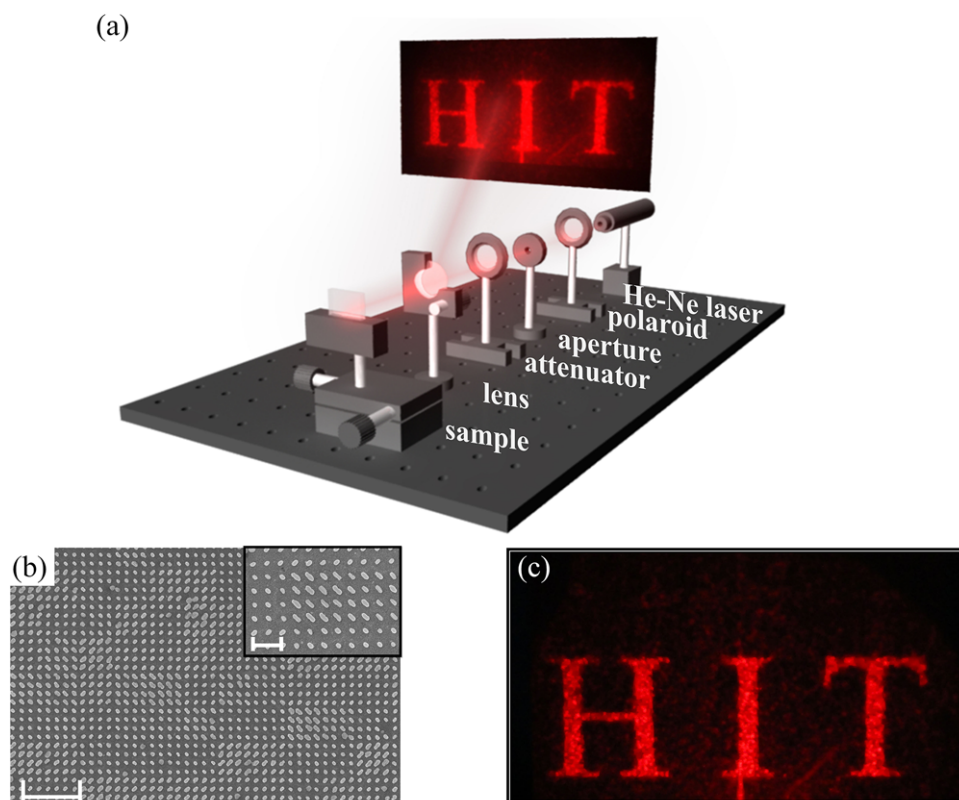


Figure 5. The perovskite holographic image. a) The schematic picture of the perovskite metasurface based hologram in a reflection mode. b) The top-view SEM image of the MAPbBr₃ perovskite based metasurface. The scale bar is 3 μm. The inset shows the high resolution SEM of perovskite metasurface with 1 μm scale bar. c) is the experimentally recorded holographic image “HIT” from MAPbBr₃ perovskite metasurface.

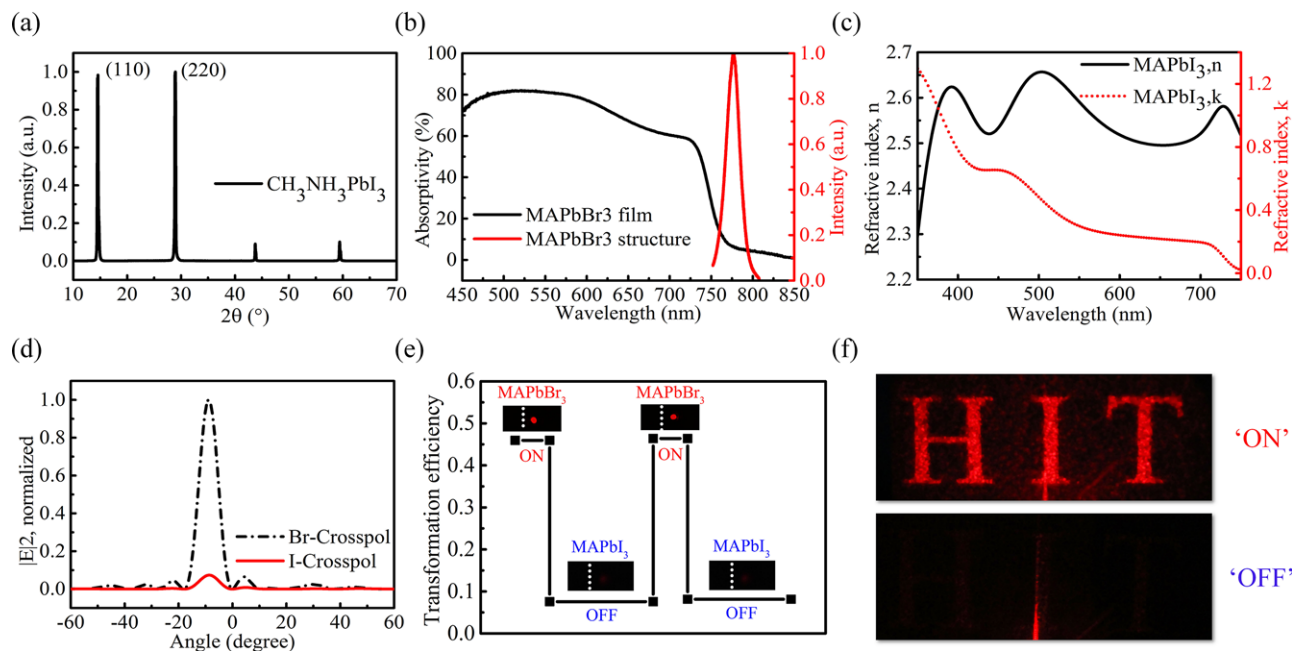


Figure 6. Dynamic holographic image. a) The XRD spectra for the as-grown MAPbI₃ perovskite film. b) and c) show the corresponding absorption and fluorescence spectra and n , k of MAPbI₃ perovskite films. d) The calculated far field angular distributions of anomalous reflection from MAPbBr₃ metasurface (dashed line) and MAPbI₃ metasurface (solid line). e) The experimentally recorded “ON” and “OFF” of the anomalous reflection. The insets are their corresponding reflection images. f) The experimentally recorded holographic image “HIT” in with “ON” and “OFF” from MAPbBr₃ perovskite metasurface and converted MAPbI₃ perovskite metasurface, respectively.

new peaks emerged at 14.58° , 28.94° , 43.76° , and 59.42° , which could be indexed to the crystal planes of MAPbI₃ perovskites. Meanwhile, the bandgap of perovskite film also moved from 2.25 eV to 1.6 eV (see Figure 6b), clearly confirming the complete transition from MAPbBr₃ perovskite to MAPbI₃ perovskite. The solid and dashed lines in Figure 6c show the recorded n and k . After the anion exchange, the refractive index still remained at relatively large value, the light extinction ratio k significantly increased. In principle, the increased absorption can simply erase the designed functions of metasurface in the visible spectrum. In this sense, considering the precise and reversibly control of anion exchange, the perovskite-based metasurfaces are nice candidates for all-dielectric dynamic meta-devices.

Based on the n and k in Figure 6c, we tested the perovskite metasurface based anomalous reflection. The numerically calculated result is plotted as solid line in Figure 6d, where the coefficient for MAPbBr₃ perovskite is plotted as dashed line for a direct comparison. While the angles of anomalous reflection are very close, the anomalous reflectance drastically reduced to $<1/10$ of initial value when the MAPbBr₃ perovskites were transferred to MAPbI₃ perovskites. This kind of transition has also been experimentally verified. The steps in Figure 6e show the reversible transition between “ON” and “OFF” status of the MAPbX₃ perovskite metasurface. After the transition to MAPbI₃ perovskite, the absorption at 633 nm was greatly enhanced, whereas the refractive index was close.^[38] As a result, the phase shifts were well preserved but the intensity was significantly reduced from 46% to 7%. This switching off process can also be seen from the recorded photographs. As the insets shown in Figure 6e, the position of anomalous reflection spot was still kept at $r = 8.91^\circ$, and

its intensity was barely seen. Interestingly, the transition between MAPbBr₃ perovskite and MAPbI₃ perovskite is reversible. In our experiment, the efficiency of anomalous reflection has been fully recovered after converting the MAPbI₃ back to MAPbBr₃ perovskites. Therefore, the experimental results in Figure 6e clearly confirmed the potential of lead halide perovskite in dynamic meta-devices, making the dielectric metasurface comparable to their plasmonic counterparts.

The dynamic control technique via anion exchange is also applicable to the perovskite based CGH. Similar to the anomalous reflection, the dominate changes happened in the light extinction coefficient (k) after the anion exchange. In this sense, the designed image shall be preserved and the intensity is reduced from $>20\%$ to $<2\%$ when the MAPbBr₃ was transferred to MAPbI₃. This is exactly what we have observed in experiment. As shown in Figure 6f, the holographic image “HIT” has been almost fully erased and only the diffracted light from central point can be seen. Owing to the unique property of MAPbX₃ perovskites, the perovskite-based meta-hologram has also been switched from “OFF” state to “ON” state by converting the MAPbI₃ perovskite back to MAPbBr₃ perovskite, making the perovskite meta-hologram dynamically and reversibly switchable. Note that the “OFF” state absorbed most of incident laser. However, the perovskite metasurface only produced photoluminescence instead of lasing under continuous excitation at room temperature.^[51] As a result, the near-infrared photoluminescence did not change the hologram patterns in Figure 6f.

Till now, based on the experimental results on both of dynamic anomalous reflection and dynamic hologram, we confirm that lead halide perovskite can be a nice platform to fill the gap

between dielectric metasurface with complete phase control and dynamic functions, which are only attainable in plasmonic metasurface very recently.^[27] The “ON-state” is operating in the transparent spectral range and experience very low absorption loss. Meanwhile, according to the recent developments, the transition time can be as short as tens of seconds or below one second if the other anion exchange techniques are applied.^[59–61] Remarkably, lead halide perovskites have shown exceptional nonlinear properties, making the nonlinear meta-devices attainable. All these performances simply make perovskite metasurfaces superior than the previous reports.

3. Conclusion

In summary, we have experimentally demonstrated the MAPbX₃ perovskite-based metasurfaces with a complete control of phase shift in a reflection mode. By patterning MAPbBr₃ cut-wires as meta-atoms on a ground metal film, we find that the MAPbBr₃ perovskite metasurface can produce full phase control from 0 to 2 π and high reflection efficiency simultaneously. Consequently, high-efficiency polarization conversion ($\approx 45\%$ for absolute efficiency, $\approx 80\%$ for conventional definition), anomalous reflection ($\approx 45\%$), and hologram ($\approx 22\%$) have been experimentally realized. These values can be further improved by using single-crystalline lead halide perovskite microplates or film to replace the polycrystalline film. Importantly, by post-synthetically and reversibly control the optical properties of MAPbX₃, we have demonstrated that the metasurface based anomalous reflection and hologram can be simply switched “ON” and “OFF” via anion exchange. Our study is the experimental realization of dynamic all-dielectric metasurface in the visible spectrum. It can pave a new route to the dynamic metasurfaces and dynamic meta-devices. This research can also expand the practical applications of perovskites from conventional optoelectronics to meta-devices such as dynamic anomalous reflection, dynamic lens, and dynamic hologram.

4. Experimental Section

Deposition of Au and SiO₂ Films: The Au and SiO₂ films were deposited onto glass substrate with E-beam evaporation (SKE.A.75). The base vacuum pressure was 2×10^{-7} Torr. The deposition rates of Au and SiO₂ were 0.4 and 0.5 Å s⁻¹, respectively. After the deposition of SiO₂, the substrate was treated with oxygen plasma (MYCRO, FEMTO6SA) for 12 s to achieve the hydrophilic surface.

Preparation of Perovskite Films: The MAPbX₃ perovskite film was prepared by spin-coating the MAPbX₃ precursor onto a substrate coated with Au and SiO₂. The MAPbX₃ precursor was obtained by dissolving PbBr₂ and CH₃NH₃Br (99.999%, Shanghai MaterWin New Materials co.) with a 1:1 molar ratio in dimethylsulfoxide. The solution was stirred for 6 h and filtrated by 0.2 μ m polytetrafluoroethylene (PTFE) syringes before use. To get the perovskite film with a thickness of 220 nm, the 35 μ L 1.2 M CH₃NH₃PbBr₃ precursor was spin-coated onto the Au layer at 4000 rpm for 90 s. At the 23rd second of spinning, 70 μ L of chlorobenzene was quickly dropped on the film to promote formation of uniform and dense lead halide perovskite film. And for the thickness of 300 nm, that is 1.4 M precursor at 3500 rpm for 90 s and chlorobenzene was dropped at the 27th second. Notably, the above prepared process was conducted in the glovebox with Ar₂ gas at room temperature.

Fabrication of Perovskite Metasurfaces: The MAPbBr₃ metasurfaces includes an electron-beam lithography and an inductively coupled plasma etching. 400 nm electron-beam resist (ZEP-520A) was spin-coated onto the perovskite film and then patterned by electron beam writer (Raith E-line) with a dose 90 C cm⁻² under an acceleration voltage 30 kV. After developing in N50, the pattern of metasurface was generated in the E-beam resist. The pattern was transferred to MAPbBr₃ perovskite with an etching process (Oxford Instruments, PlasmaPro ICP180). The vacuum degree was 10⁻⁹. The ICP power was 600 W, and the RF power was 150 W. Under this condition, the MAPbBr₃ film was etched by chlorine gas with 5 sccm flow rate. C₄F₈ with 10 sccm flow rate was used as protective gas.

Optical Characterization: The anomalous reflection and hologram of perovskite metasurface were characterized with a homemade optical setup. The details are shown as Figure S3, Supporting Information. During the optical measurements, both of co-polarized light and cross-polarized light were characterized and their intensities were I_N and I_A , respectively. Next, the intensity from a pure Au mirror was measured as the total input power (I_{Au}). Thus, the anomalous reflectance η ($\eta = I_A/I_{Au}$) was calculated. Similar method is also used for the characterization of hologram image.

Conversion between MAPbBr₃ and MAPbI₃: The MAPbBr₃ perovskite was converted to MAPbI₃ perovskite in a CVD tube. During the whole vapor conversion process, the MAI powder was placed at the center of the CVD furnace while the MAPbBr₃ patterns which have already prepared on the substrate were mounted downstream of the apparatus. The central heating zone was increased to 125 °C (8 °C min⁻¹ heating rate, 10 min as buffer) under low-pressure conditions (40–50 Torr) and maintained from 25 min to 2 h. Ar and H₂ were used as carrier gases with flow rates of 35 and 15 sccm, respectively. The furnace was then naturally cooled to room temperature and MAPbI₃ microplates have been obtained. The reversed conversion process is similar.

Numerical Simulations: Full-wave numerical simulations of near fields were carried out by using the commercial finite-element method solver COMSOL Multiphysics. The calculated geometries were taken from experimentally obtained SEM images. The dielectric permittivity of the silica substrate was 2.25, whereas the optical properties of the perovskite film have a strong dispersion and has been considered (See Figure S4, Supporting Information). The maximum value of permittivity of the perovskite was about 6.5, which is much larger as compared with values for the substrate and air, providing a high optical contrast for Mie resonance excitation.

Supporting Information

Supporting Information is available from the Wiley Online Library or from the author.

Acknowledgements

This research was financially supported by National Key Research and Development Program of China Grant No. SQ2018YFB220027 and National Natural Science Foundation of China under the grant No. 91850204 and Shenzhen Fundamental research projects under the grant No. JCYJ20180507183532343.

Conflict of Interest

The authors declare no conflict of interest.

Keywords

anomalous reflection, dynamic control, holograms, lead halide perovskites, metasurfaces

Received: March 5, 2019
Revised: May 12, 2019
Published online: June 11, 2019

- [1] N. Yu, P. Genevet, M. A. Kats, F. Aieta, J.-P. Tetienne, F. Capasso, Z. Gaburro, *Science* **2011**, 334, 333.
- [2] X. Ni, N. K. Emani, A. V. Kildishev, A. Boltasseva, V. M. Shalaev, *Science* **2012**, 335, 427.
- [3] L. Huang, X. Chen, H. Mühlenbernd, G. Li, B. Bai, Q. Tan, G. Jin, T. Zentgraf, S. Zhang, *Nano Lett.* **2012**, 12, 5750.
- [4] F. Aieta, P. Genevet, N. Yu, M. A. Kats, Z. Gaburro, F. Capasso, *Nano Lett.* **2012**, 12, 1702.
- [5] X. Yin, Z. Ye, J. Rho, Y. Wang, X. Zhang, *Science* **2013**, 339, 1405.
- [6] M. I. Shalaev, J. Sun, A. Tsukernik, A. Pandey, K. Nikolskiy, N. M. Litchinitser, *Nano Lett.* **2015**, 15, 6261.
- [7] A. Arbabi, Y. Horie, M. Bagheri, A. Faraon, *Nat. Nanotechnol.* **2015**, 10, 937.
- [8] F. Monticone, N. M. Estakhri, A. Alù, *Phys. Rev. Lett.* **2013**, 110, 203903.
- [9] J. P. B. Mueller, K. Leosson, F. Capasso, *Optica* **2016**, 3, 42.
- [10] L. L. Li, T. J. Cui, W. Ji, S. Liu, J. Ding, X. Wan, Y. B. Li, M. Jiang, C.-W. Qiu, S. Zhang, *Nat. Commun.* **2017**, 8, 197.
- [11] C. Qu, S. Ma, J. Hao, M. Qiu, X. Li, S. Xiao, Z. Miao, N. Dai, Q. He, S. Sun, L. Zhou, *Phys. Rev. Lett.* **2015**, 118, 113901.
- [12] B. Wang, F. Dong, Q. T. Li, D. Yang, C. Sun, J. Chen, Z. Song, L. Xu, W. Chu, Y.-F. Xiao, Q. Gong, Y. Li, *Nano Lett.* **2016**, 16, 5235.
- [13] D. Lin, P. Fan, E. Hasman, M. Brongersma, *Science* **2014**, 345, 298.
- [14] X. Zhu, W. Yan, U. Levy, N. A. Mortensen, A. Kristensen, *Sci. Adv.* **2017**, 3, e1602487.
- [15] J. Tian, H. Luo, Q. Li, X. Pei, K. Du, M. Qiu, *Laser Photonics Rev.* **2018**, 12, 1800076.
- [16] M. Khorasaninejad, W. T. Chen, R. C. Devlin, J. Oh, A. Zhu, F. Capasso, *Science* **2016**, 352, 1190.
- [17] S. Colburn, A. Zhan, A. Majumdar, *Sci. Adv.* **2018**, 4, eaar2114.
- [18] B. Chen, P. Wu, V. Su, Y. Lai, C. Chu, I. Lee, J. Chen, Y. Chen, Y. Lan, C. Kuan, D. Tsai, *Nano Lett.* **2017**, 17, 6345.
- [19] S. Wang, P. C. Wu, V.-C. Su, Y. C. Lai, M. K. Chen, S. Y. Kuo, B. H. Chen, Y. H. Chen, T. T. Huang, J.-H. Wang, R. L. Lin, C. H. Kuan, T. Li, Z. Wang, S. Zhu, D. P. Tsai, *Nat. Nanotechnol.* **2018**, 13, 227.
- [20] W. T. Chen, A. Y. Zhu, V. Sanjeev, M. Khorasaninejad, Z. Shi, E. Lee, F. Capasso, *Nat. Nanotechnol.* **2018**, 13, 220.
- [21] S. Sun, Z. Zhou, C. Zhang, Y. Gao, Z. Duan, S. Xiao, Q. Song, *ACS Nano* **2017**, 11, 4445.
- [22] M. A. Gorchak, X. Ni, D. A. Smirnova, D. Korobkin, D. Zhirihin, A. P. Slobozhanyuk, P. A. Below, A. Alù, A. B. Khanikaev, *Nat. Commun.* **2018**, 9, 909.
- [23] A. Howes, W. Wang, I. Kravchenko, J. Valentine, *Optica* **2018**, 7, 787.
- [24] S. C. Malek, H.-S. Ee, R. Agarwal, *Nano Lett.* **2017**, 17, 3641.
- [25] X. Duan, S. Kamin, N. Liu, *Nat. Commun.* **2017**, 8, 14606.
- [26] Y.-W. Huang, H. W. H. Lee, R. Sokhoyan, R. A. Pala, K. Thyagarajan, S. Han, D. P. Tsai, H. A. Atwater, *Nano Lett.* **2016**, 16, 5319.
- [27] J. Li, S. Kamin, G. Zheng, F. Neubrech, S. Zhang, N. Liu, *Sci. Adv.* **2018**, 4, eaar6768.
- [28] M. Papaioannou, E. Plum, E. T. F. Rogers, N. I. Zheludev, *Light: Sci. Appl.* **2018**, 7, 17157.
- [29] S. Sun, W. Yang, C. Zhang, J. Jing, Y. Gao, X. Yu, Q. Song, S. Xiao, *ACS Nano* **2018**, 12, 2151.
- [30] J. Bohn, T. Bucher, K. E. Chong, A. Komar, D.-Y. Choi, D. N. Neshev, Y. S. Kivshar, T. Pertsch, I. Staude, *Nano Lett.* **2018**, 18, 3461.
- [31] B. R. Sutherland, E. H. Sargent, *Nat. Photonics* **2016**, 10, 295.
- [32] M. A. Green, A. Ho-Baillie, H. J. Snaith, *Nat. Photonics* **2014**, 8, 506.
- [33] NREL efficiency chart, <http://www.nrel.gov/pv/assets/images/efficiency-chart.png> (accessed: June 2018).
- [34] L. Dou, Y. Yang, J. You, Z. Hong, W.-H. Chang, G. Li, Y. Yang, *Nat. Commun.* **2014**, 5, 5404.
- [35] G. C. Xing, N. Mathews, S. S. Lim, N. Yantara, X. F. Liu, D. Sabba, M. Grätzel, S. Mhaisalkar, T. C. Sum, *Nat. Mater.* **2014**, 13, 476.
- [36] H. M. Zhu, Y. P. Fu, F. Meng, X. Wu, Z. Gong, Q. Ding, M. V. Gustafsson, M. T. Trinh, S. Jin, X.-Y. Zhu, *Nat. Mater.* **2015**, 14, 636.
- [37] S. W. Eaton, M. Lai, N. A. Gibson, A. B. Wong, L. Dou, J. Ma, L.-W. Wang, S. R. Leone, P. Yang, *Proc. Natl. Acad. Sci. USA* **2016**, 113, 1993.
- [38] H. Huang, J. Raith, S. V. Kershaw, S. Kalytchuk, O. Tomanec, L. Jing, A. S. Susha, R. Zboril, A. L. Rogach, *Nat. Commun.* **2017**, 8, 996.
- [39] S. D. Stranks, H. J. Snaith, *Nat. Nanotechnol.* **2015**, 10, 391.
- [40] Q. Zhang, S. T. Ha, X. Liu, T. C. Sum, Q. Xiong, *Nano Lett.* **2014**, 14, 5995.
- [41] Y. Fang, Q. Dong, Y. Shao, Y. Yuan, J. Huang, *Nat. Photonics* **2015**, 9, 679.
- [42] R. Su, C. Diederichs, J. Wang, T. C. H. Liew, J. Zhao, S. Liu, W. Xu, Z. Chen, Q. Xiong, *Nano Lett.* **2017**, 17, 3982.
- [43] K. B. Lin, J. Xing, L. N. Quan, F. P. García de Arquer, X. W. Gong, J. X. Lu, L. Q. Xie, W. J. Zhao, D. Zhang, C. Z. Yan, W. Q. Li, X. Y. Liu, Y. Lu, J. Kirman, E. H. Sargent, Q. H. Xiong, Z. H. Wei, *Nature* **2018**, 562, 245.
- [44] Y. Cao, N. N. Wang, H. Tian, J. S. Guo, Y. Q. Wei, H. Chen, Y. F. Miao, W. Zou, K. Pan, Y. R. He, H. Cao, Y. Ke, M. M. Xu, Y. Wang, M. Yang, K. Du, Z. W. Fu, D. C. Kong, D. X. Dai, Y. Z. Jin, G. Q. Li, H. Li, Q. M. Peng, J. P. Wang, W. Huang, *Nature* **2018**, 562, 249.
- [45] N. Zhang, Y. B. Fan, K. Y. Wang, Z. Y. Gu, Y. H. Wang, L. Ge, Q. H. Song, S. M. Xiao, *Nat. Commun.* **2019**, 10, 1770.
- [46] Y. B. Fan, Y. H. Wang, N. Zhang, W. Z. Sun, C.-W. Qiu, Q. H. Song, S. M. Xiao, *Nat. Commun.* **2019**, 10, 2085.
- [47] B. Gholipour, G. Adamo, D. Cortecchia, H. N. S. Krishnamoorthy, M. D. Birowosuto, N. I. Zheludev, C. Soci, *Adv. Mater.* **2017**, 29, 1604268.
- [48] S. V. Makarov, V. Milichko, E. V. Ushakova, M. Omelyanovich, A. C. Pasaran, R. Haroldson, B. Balachandran, H. Wang, W. Hu, Y. S. Kivshar, A. A. Zakhidov, *ACS Photonics* **2017**, 4, 728.
- [49] Y. Gao, C. Huang, C. Hao, S. Sun, L. Zhang, C. Zhang, Z. Duan, K. Wang, Z. Jin, N. Zhang, A. V. Kildishev, C.-W. Qiu, Q. Song, S. Xiao, *ACS Nano* **2018**, 12, 8847.
- [50] M. A. Green, Y. Jiang, A. M. Soufiani, A. Ho-Baillie, *J. Phys. Chem. Lett.* **2015**, 6, 4774.
- [51] Y. Jia, R. A. Kerner, A. J. Grede, B. P. Rand, N. C. Giebink, *Nat. Photon.* **2017**, 11, 784.
- [52] N. Zhang, W. Sun, S. P. Rodrigues, K. Wang, Z. Gu, S. Wang, W. Cai, S. Xiao, Q. Song, *Adv. Mater.* **2017**, 29, 1606205.
- [53] M. S. Alias, Y. Yang, T. K. Ng, I. Dursun, D. Shi, M. I. Saidaminov, D. Priante, O. M. Bakr, B. S. Ooi, *J. Phys. Chem. Lett.* **2016**, 7, 137.
- [54] E. Y. Tiguntseva, G. P. Zograf, F. E. Komissarenko, D. A. Zuev, A. A. Zakhidov, S. V. Makarov, Kivshar, *Nano Lett.* **2018**, 18, 1185.
- [55] Z. Duan, Y. Wang, G. Li, S. Wang, N. Yi, S. Liu, S. Xiao, Q. Song, *Laser Photonics Rev.* **2018**, 12, 1700234.
- [56] Q. Liao, K. Hu, H. Zhang, X. Wang, J. Yao, H. Fu, *Adv. Mater.* **2015**, 27, 3405.
- [57] Y. Yang, W. Wang, P. Moitra, I. I. Kravchenko, D. P. Briggs, J. Valentine, *Nano Lett.* **2014**, 14, 1394.
- [58] E. Y. Tiguntseva, D. G. Baranov, A. P. Pushkarev, B. Munkhbat, F. Komissarenko, M. Franckevičius, A. A. Zakhidov, T. Shegai, Y. S. Kivshar, S. V. Makarov, *Nano Lett.* **2018**, 18, 5522.
- [59] N. Zhang, K. Wang, H. Wei, Z. Gu, W. Sun, J. Li, S. Xiao, Q. Song, *J. Phys. Chem. Lett.* **2016**, 7, 3886.
- [60] L. Dou, M. Lai, C. S. Kley, Y. Yang, C. G. Bischak, D. Zhang, S. W. Eaton, N. S. Ginsberg, P. D. Yang, *Proc. Nat. Acad. Sci. USA* **2017**, 114, 7216.
- [61] N. Pellet, J. Teuscher, J. Maier, M. Gratzel, *Chem. Mater.* **2015**, 27, 2181.